Acta Neuropathologica Communications

RESEARCH

Open Access

Anlotinib may have a therapeutic effect on papillary craniopharyngiomas without the BRAFv600e mutation

Yilamujiang Ainiwan[1†], Haomin Li[1,2†], Yongjia Zheng[3†], Songtao Wei[1†], Junxiang Peng[1], Jing Nie[1], Chaofu Mao[4], Kunxiang Chen[1], Siyuan Chen[1], Ningyuan Liu[5], Can Li[6], Yan Chen[1], Shanqiang Qu[1], Yunji Wang[1], Mingfeng Zhou[1], Jian Mao[1], Fen Mei[1], Jingting Chen[7], Qiancheng Song[1*], Songtao Qi[1*] and Jun Pan[1*]

Abstract

Background Although successful treatment of papillary craniopharyngiomas (PCPs) with BRAFv600e inhibitors has been reported in clinical trials, studies have shown that approximately 10% of PCPs lack the BRAFv600e mutation and that BRAFv600e inhibitors may not be significantly effective against these tumors. However, no studies have focused specifically on BRAFv600e^{-} PCPs.

Methods Spatial transcriptome sequencing was performed on calcified PCP tissue to identify novel subtypes of PCP cells. The findings were validated via pathological methods in 51 PCP samples. Primary PCP cells from BRAFv600e^{-} PCP patients and BRAFv600e^{+} PCP patients were isolated and then injected into the brains of nude mice via stereotactic surgery to establish a stable mouse model of human-originated PCP. Model mice were treated with vemurafenib, a BRAF inhibitor, and anlotinib, an angiogenesis inhibitor. BRAFv600e^{-}PCP patients were treated with anlotinib in a phase 1 clinical trial. Changes in the tumors of the model mice and patients were monitored via pathological methods, CT and MRI.

Results Most of calcified PCPs were negative for the BRAFv600e mutation, and findings from the mouse model confirmed that vemurafenib may not have a significant therapeutic effect on BRAFv600e^{-} PCPs. However, the mouse model verified that, anlotinib may have a significant therapeutic effect on BRAFv600e^{-} PCPs. Two patients with BRAFv600e^{-} PCPs participated in a phase 1 clinical trial and received anlotinib therapy; their tumors disappeared after 3 months of therapy and did not recur within 24 months follow-up after stopping the treatment.

†Yilamujiang Ainiwan, Haomin Li, Yongjia Zheng and Songtao Wei contributed equally to this work.

*Correspondence:
Qiancheng Song
songqc@smu.edu.cn
Songtao Qi
qisongtaosjwk@163.com
Jun Pan
1448875873@qq.com

Full list of author information is available at the end of the article

Conclusion BRAFv600e⁻ PCPs are characterized by calcification and do not respond to the BRAF inhibitor vemurafenib, and for which the angiogenesis inhibitor anlotinib may have a significant therapeutic effect.

Keywords Papillary craniopharyngioma, BRAFv600e mutation, Calcification, Vemurafenib, Anlotinib

Introduction

Craniopharyngioma (CP) is a tumor of epithelial origin that arises from the metaplasia of cells remaining from embryonic Rathke cleft cysts (RCC); although the vast majority of CPs exhibit WHO grade I pathology, CP often invades the neighboring hypothalamus or pituitary gland, causing fatal complications that are difficult to ameliorate by surgery [1]. Researchers have long believed that there are 2 pathologic subtypes of CP: adamantinomatous craniopharyngioma (ACP) and papillary craniopharyngioma (PCP) [2]. However, these entities greatly differ in many ways. For example, in terms of age of onset, ACP diagnosis exhibits a bimodal peak of incidence at 5–15 years and 45–60 years, whereas PCPs are restricted to adults, mainly at 40–60 years. On imaging, calcification is present in more than 90% of ACPs and very rarely in PCPs [1, 3]. Pathologically, ACPs are characterized by cluster cells (epithelial whorls), palisading epithelium, stellate reticulum, wet keratin, cystic cavities, and calcifications, whereas PCPs have only papillary raised squamous epithelium, occasional cystic cavities, and no other characteristic structures [1, 4]. Etiologically, ACPs are caused mainly by mutations in the CTNNB1 gene (encoding beta-catenin) in cluster cells, resulting in abnormal aggregation of oncogenic beta-catenin in the nucleus of cluster cells and subsequent tumorigenesis induced by senescent cluster cells [1]. Martinez et al. [5] found that a complex interplay between cellular senescence, cytokine signaling, and gene expression pathways underlies ACP development by using multimodal machine learning analysis.It has also been suggested that ACPs may result from activation of the MAPK/ERK pathway [6]. Recent studies have revealed that ACP development may involve a mechanism similar to that of senescence-related neurodegenerative diseases [7, 8]. However, PCPs may be formed by Rax + tanycytes with a BRAFv600e mutation in the median eminence of the hypothalamus, and approximately 90% of PCPs carry the BRAFv600e mutation [1, 3, 9] and exhibit beta-catenin localization to the cell membrane or cytoplasm rather than the nucleus [10]. The annual incidence of ACP is approximately 0.5–2 per million people, whereas the incidence of PCP is approximately 1/10 that of ACP [1, 11]. A recent study have revealed the differences in the cellular composition and spatial distribution between ACP and PCP [12].Therefore, in 2021, the WHO classified these tumors as completely different rather than different subtypes of the same tumor [13]. The calcification of PCP is very rare, and no mechanistic studies have investigated its occurrence. Moreover, approximately 10% of PCPs lack the BRAFv600e mutation. However, no studies have focused specifically on BRAFv600e⁻ PCPs.

Although recent studies about spatial transcriptome sequencing on ACPs have revealed new subtypes of ACP cells and potential therapeutic targets [5, 14–16], few of them focused on PCPs via spatial transcriptome sequencing.In this study, a special PCP patient presented with imaging-visible calcification of the tumor. To our knowledge, calcification in PCPs is very rare, and the mechanism is still unclear, therefore, we performed spatial transcriptome sequencing on these calcified PCP tumor samples to explore their biological characteristics. We identified new subclusters of PCP cells that have the potential for calcification, very similar to that of ACPs. During data validation on many PCP samples, we identified another 3 cases of calcified PCPs. This study revealed that calcified PCPs have similar histological and pathological characteristics to ACPs, and most of them (3 in 4 cases) were negative for the BRAFv600e mutation, implying that BRAF inhibitors may not have a therapeutic effect on these BRAFv600e⁻ PCPs. To validate the efficacy of a BRAF inhibitor on BRAFv600e⁻ PCPs, we established a novel human PCP xenograft mouse model by injecting primary PCP cells obtained from patients into the brains of nude mice, addressing the previous absence of a stable mouse model of human-origin PCP, which may provide a reliable animal model for the exploration of new therapeutic targets for PCPs. The poor response of BRAFv600e⁻ PCPs to vemurafenib, a common BRAF inhibitor, was verified in the PCP mouse model. Moreover, we revealed that the classical angiogenesis promoter PDGFR was widely expressed in both BRAFv600e⁻ PCPs and BRAFv600e⁺ PCPs, and the PCP mouse model confirmed that anlotinib, a common PDGFR inhibitor that acts as an antiangiogenic agent, had a significant therapeutic effect on BRAFv600e⁻ PCPs.

Finally, we initiated a phase 1 clinical trial for anlotinib therapy in BRAFv600e⁻ PCP patients and presented the first report of the successful and clinical cure of patients with BRAFv600e⁻ PCPs via anlotinib.

In conclusion, we report for the first time that BRAFv600e⁻ PCPs are characterized by calcification and do not respond to the BRAF inhibitor vemurafenib, and for which the angiogenesis inhibitor anlotinib may have a significant therapeutic effect.

Materials and methods

This information is provided in Supplementary File 1t.

Results

New subtypes of PCP cells and their spatial distributions were identified in calcified PCP tumor tissue via spatial transcriptome sequencing

To explore the mechanisms of calcification in PCPs, we performed spatial transcriptome sequencing on 1 PCP tumor sample with imaging-visible calcification (Fig. 1 A). Seven clusters were determined according to the spatial distribution of marker genes for each cluster (Fig. 1 B). Each spot in the figure is a single gene capture unit, and each spot in the tissue includes 1–10 cells. The number of spots in the tissue was 2957, the mean number of reads per spot was 97,833, and the median number of genes per spot was 2496. The number of genes with at least one UMI in any tissue-covered spot was 22,000, which was the total number of detected genes (Fig. 1 B). Cluster 0, Cluster 1, Cluster 3, and Cluster 4 specifically expressed CTNNB1, one of the classical marker genes for PCP, as well as the marker genes CDH1 and CDH3 for epithelial cells; therefore, these clusters were defined as PCP cells and named PCP-1, PCP-2, PCP-3, and PCP-4, respectively (Fig. 1 C). Notably, PCP-2 and PCP-3 also specifically expressed ODAPH and BMP2 (Fig. 1 C), which are expressed in ACPs that positively regulate calcification and have not been previously identified in PCPs. Cluster 2 specifically expressed NFAT5, NPIPB5

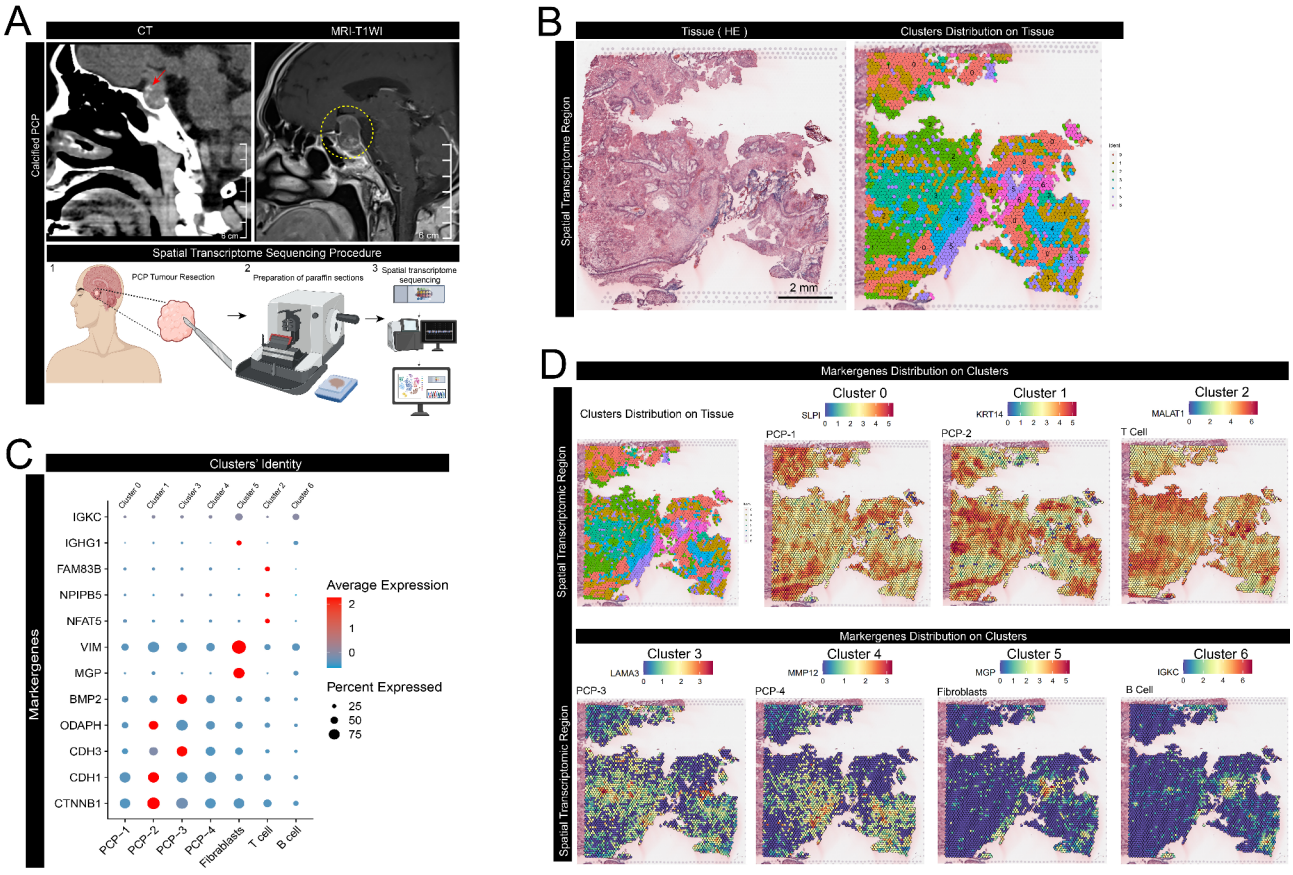

Fig. 1 New subtypes of PCP cells and their spatial distributions were identified in calcified PCP tumor tissue via spatial transcriptome sequencing. **A**: Imaging features of calcified PCPs used for spatial transcriptome sequencing. The red arrow indicates calcification in the tumor on CT imaging. The yellow dotted box indicates the PCP tumor with its solid component and cystic cavity on MRI. The procedures of spatial transcriptome sequencing are shown in steps 1 to 3 (created in Biorender). www.biorender.com). **B**: HE staining of spatial transcriptomic regions of the PCP sample; the area within the dashed box is the gene capture region. The map of spatial location indicates the distribution of each cluster on the tissue. The locations of the seven clusters were determined according to the spatial distribution of marker genes for each cluster. Each spot in the figure is a single gene capture unit, and each spot in the tissue includes 1–10 cells. The number of spots in the tissue was 2957, the mean number of reads per spot was 97833, and the median number of genes per spot was 2496. The number of genes with at least one UMI count in any tissue-covered spot is 22000, which is the total number of detected genes. **C**: All the spots captured in the tumor specimen were divided into 7 clusters according to the expression of specific marker genes in each cluster. Cluster 0, Cluster 1, Cluster 3, and Cluster 4 specifically expressed CTNNB1, one of the classical marker genes for PCP, as well as the marker genes CDH1 and CDH3 for epithelial cells; therefore, these clusters were defined as PCP cells and named PCP-1, PCP-2, PCP-3, and PCP-4. Cluster 2 specifically expressed the T-cell marker genes NFAT5, NPIPB5 and FAM83B. Cluster 5 specifically expressed the fibroblast markers MGP and VIM. Cluster 6 specifically expressed the B-cell marker genes IGHG1 and IGKC. **D**: Spatial map for the cell clustering heatmap showing the marker gene expression level and specificity; a deeper red color indicates a higher expression level of the marker gene for that cluster. The spatial location of each cluster's markergene is highly consistent with the spatial distribution of the clusters in a given tissue

and FAM83B, which are common marker genes of T cells (Fig. 1 C). Cluster 5 specifically expresses MGP and VIM, which are marker genes of fibroblasts, and Cluster 6 specifically expresses IGHG1 and IGKC, which are marker genes of B cells (Fig. 1 C). Thus, cell types were identified for all clusters in the PCP tumor specimen.

To further clarify the potential function of each cluster, we annotated the top 10 genes expressed by each cluster and plotted a heatmap of the PCP spatial transcriptional sequencing data (Supplementary Fig. 1 A). PCP-1 (Cluster 0) showed specific high expression of SLPI, which promotes epithelial cell formation; PCP-2 (Cluster 1) showed specific high expression of KRT14, a gene encoding type 1 keratin; PCP-3 (Cluster 3) showed specific high expression of the keratin-promoting gene LAMA3 and the enamel-promoting gene ODAPH; PCP-4 (Cluster 4) showed specific high expression of MMP12 and KRT13, which promote cell adhesion and proliferation; T cells (Cluster 2) showed specific high expression of MALAT1; fibroblasts (Cluster 5) specifically expressed MGP and VIM, which are marker genes of fibroblasts; and B cells (Cluster 6) presented specific high expression of IGHG1 and IGKC, which encode immunoglobulins (Supplementary Fig. 1 A). The spatial locations of the markers for each cluster were highly consistent with the spatial locations of the corresponding clusters (Fig. 1 D). These results suggest that each subtype of calcified PCP cells has a unique function, specifically, epithelial formation, calcification and proliferation.

Pseudotime analysis revealed distinct cell fates and the potential for PCP cell subtype calcification during development

The discovery of PCP subclusters carrying calcification-related genes led us to explore the fate of these subclusters. Pseudotime analysis of all the PCP subclusters (Cluster 0, Cluster 1, Cluster 3, and Cluster 4) was performed via Monocle 2 software. The results revealed that PCP subclusters undergo differentiation from Cluster 0 → Cluster 4 → Cluster 3 → Cluster 1 during development (Fig. 2 A). The CytoTRACE_Score scores revealed that Cluster 0 had the lowest CytoTRACE score and the strongest capacity for differentiation, whereas Cluster 1 had the highest CytoTRACE score and the weakest differentiation capacity, further confirming the direction of cell differentiation from Cluster 0 to Cluster 1 (Fig. 2 B-C).

To clarify the cell fate of PCP subclusters after differentiation, this study used the differential GeneTest function of Monocle2 to identify genes whose expression patterns changed over pseudotime, drew a heatmap of the differentially enriched genes to obtain gene clusters, and performed GO enrichment analysis of each of the 3 obtained clusters. The results revealed that each cluster presented distinct cell fates during differentiation (Fig. 2 D). The genes in Cluster 1 were progressively upregulated during development and were associated mainly with the upregulation of skin development, epidermal development, calcification, and cartilage development, which are very similar to those in ACPs (Fig. 2 D-E). The genes in Cluster 2 were progressively downregulated during development and were associated mainly with the downregulation of skin development, epithelial cell proliferation and intercellular junctions (Fig. 2 D-E). The genes in Cluster 3 were progressively upregulated during development and were involved mainly in ribosome assembly, positive regulation of p53, epithelial cell development and transcription initiation, which are necessary for cell proliferation (Fig. 2 D-E). Thus, the cell fate of the PCP subclusters can be summarized as follows: Cluster 1 differentiates in the direction of epithelial cell calcification, which is very similar to ACP calcification; Cluster 2 differentiates in the opposite direction of epithelial cell proliferation, i.e., in the direction of epithelial cell senescence, notably, senescence is one of the typical biological features of ACPs; and Cluster 3 differentiates in the direction of epithelial cell development and proliferation. Finally, we confirmed that the calcification-promoting genes BMP2, RUNX2 and ODAPH were expressed on calcified PCPs ($n=4$) and ACPs ($n=17$). However, the expression of BMP2, RUNX2 and ODAPH was negative in the uncalcified PCPs ($n=47$) (Supplementary Fig. 2). These results suggest that calcified PCPs may have a strong connection with ACPs and that the calcification-promoting genes BMP2, RUNX2 and ODAPH may play essential roles in PCP calcification.

Imaging, histological and pathological features of the calcified PCPs

To further validate the above data, we tested the biological features, including imaging, histology and pathology in 51 PCP tumor samples and detected imaging-visible calcification in 4 samples; 17 ACP samples were included in the control group. The calcified PCPs showed calcifications, solid components and cystic cavities of the tumors on CT and MRI, which are very similar to those of ACPs (Fig. 3 A). In terms of histology, calcified PCPs presented wet keratins, calcifications and ossifications on the tumor tissues, which are also very similar to ACP. However, cluster cells (epithelial whorls), palisading epithelium and stellate reticulum were still absent on calcified PCPs (Fig. 3 B). Pathologically, as a classical biomarker of PCPs, Pan-CK is localized to the cytoplasm, and beta-catenin is localized to the cell membrane rather than the nucleus (Fig. 3 B), implying that they are PCPs but not ACPs. In ACPs, as a control, Pan-CK was localized to the cytoplasm, but beta-catenin was localized to the nucleus rather than the cell membrane or cytoplasm (Fig. 3 B).

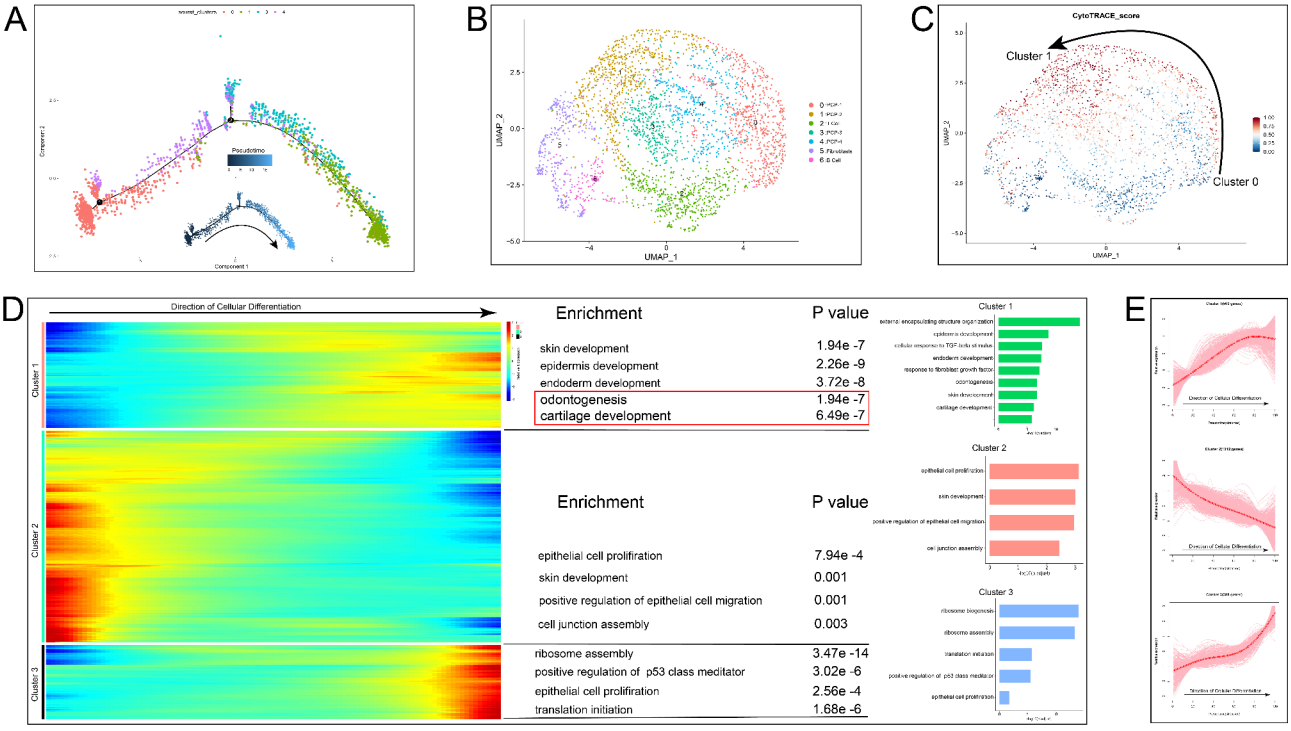

Fig. 2 Pseudotime analysis revealed distinct cell fates and the potential for calcification of PCP cell subtypes during development. **A**: Pseudotime analysis of all the PCP subclusters (Cluster 0, Cluster 1, Cluster 3, and Cluster 4) was performed via Monocle2, and pseudotime values were calculated to generate a pseudotime diagram of the PCP cell subclusters. Larger pseudotime values are shown in a lighter color and at longer distances from the initial cell point. The darker color represents the default initial cell point. Prior to the first branching point in cell development, Cluster 0 predominated, and after the first branching point, Cluster 0 gradually differentiated into Cluster 4. After the second branching point, Cluster 4 gradually differentiated into Cluster 3. As cellular differentiation continued, Cluster 3 cells eventually differentiated into Cluster 1 cells. The black arrow in the figure represents the direction of the corresponding cell differentiation trajectory, which indicates that the PCP-cultured cells gradually differentiated from Cluster 0 to Cluster 1. **B**: UMAP plot of spatial transcriptome sequencing cell clustering of the PCP sample, with closer positions between clusters in the UMAP plot indicating closer biological relationships. **C**: Prediction of the differentiation potential of each subcluster of PCP cells via CytoTRACE software. The CytoTRACE score is the predicted differentiation potential score for each cell, with lower scores (blue) representing greater cell differentiation potential and higher scores (red) indicating weaker differentiation potential. This figure shows that Cluster 0 cells have the lowest CytoTRACE_Score and the strongest differentiation capacity and that Cluster 1 cells have the highest CytoTRACE_Score and the lowest differentiation capacity. The black arrow indicates the direction of cell differentiation. **D**: The differential GeneTest function of Monocle2 was used to identify genes whose expression patterns changed over pseudotime. A heatmap of the differentially enriched genes was drawn and revealed 3 clusters, and GO enrichment analysis was performed for each cluster. The black arrow in the figure shows the direction of cell differentiation, and each cluster shows distinct cell fates during differentiation. The genes in Cluster 1 were progressively upregulated during development and were associated mainly with the upregulation of skin development, epidermal development, calcification, and cartilage development. The genes in Cluster 2 were progressively downregulated during development and were associated mainly with the downregulation of skin development, epithelial cell proliferation and intercellular junctions. The genes in Cluster 3 were progressively upregulated during development and were associated mainly with the upregulation of ribosome assembly, positive regulation of p53, epithelial cell development and transcription initiation. **E**: Visualization of GO enrichment results for the three clusters in the heatmap from panel D. The horizontal coordinates represent the pseudotime values in the pseudotime trajectories. A total of 503 genes in Cluster 1 were gradually upregulated, 1012 genes in Cluster 2 were gradually downregulated, and 389 genes in Cluster 3 were gradually upregulated with cell differentiation

Surprisingly, although the BRAFv600e mutation in exon 15, another common biomarker for PCPs, was positive in the tumors of calcified PCP patient 1, another 3 calcified PCPs were negative for the BRAFv600e mutation, as well as ACPs (Fig. 3 B). Moreover, the CTNNB1 mutation in exon 3 was negative in all calcified PCPs (Supplementary Fig. 3 A), which is strong evidence that they are PCPs but not ACPs.These findings suggest that calcified PCPs may be characterized as BRAFv600e$^-$ PCPs, implying that BRAF inhibitors may not have therapeutic effect on these PCPs.

Establishment and validation of a novel human-originated PCP mouse model

To validate the efficacy of a BRAF inhibitor on BRAFv600e$^-$ PCPs, a novel mouse xenograft model with human-origin PCPs was established in this study.

We report here, for the first time, the process of establishing and validating a human-originated PCP mouse model (see Materials and Methods for details). After primary PCP-containing cells were extracted from PCP tumor tissues, they were stored at -80 °C until pathological diagnosis and testing for BRAFv600e mutation in

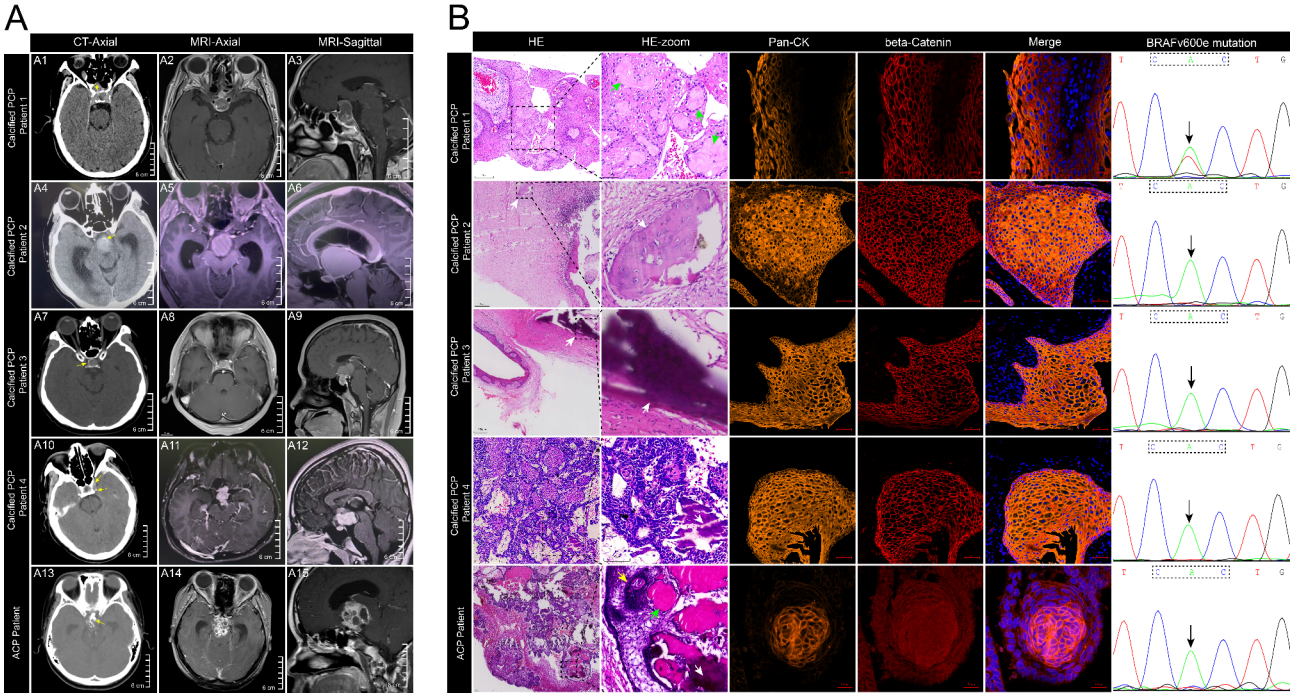

Fig. 3 Imaging, histological and pathological features of the calcified PCPs. **A**: Images from calcified PCP patients. The yellow arrows in the CT images indicate calcification of the tumors. The MR images showed the solid components and cystic cavities of the tumors. The ACP, as a control, showed calcification (yellow arrow), solid components and cystic cavity in the tumor. **B**: Histological and pathological features of the calcified PCPs. **Calcified PCP Patient 1**: the green arrows in HE staining indicate wet keratins. Pan-CK was localized to the cytoplasm, beta-catenin was localized to the membrane, and the BRAFv600e mutation was positive. **Calcified PCP Patient 2**: the white arrow in HE staining indicates calcification. Pan-CK was localized to the cytoplasm, and beta-catenin was localized to the cell membrane, but the BRAFv600e mutation was negative. **Calcified PCP Patient 3**: the white arrow in the HE image indicates ossification. Pan-CK was localized to the cytoplasm, and beta-catenin was localized to the cell membrane, but the BRAFv600e mutation was negative. **Calcified PCP Patient 4**: the white arrow in the HE-stained image indicates calcification. Pan-CK was localized to the cytoplasm, and beta-catenin was localized to the membrane rather than the nucleus, but the BRAFv600e mutation was negative. In the **ACP patient**, as a control, the ACP showed cluster cells (yellow arrow), wet keratin (green arrow) and ossification (white arrow) on HE staining. Pan-CK was localized to the cytoplasm, and beta-catenin was localized to the nucleus rather than the cell membrane, but the BRAFv600e mutation was negative

tumor tissues. Then, they were injected into the brains of the nude mice via stereotactic surgery, after which they were allowed to form tumors (Fig. 4 A). The tightly arranged squamous epithelial cells were observed under a light microscope, and beta-catenin and Pan-CK, which are biomarkers for PCP, were expressed in the cytoplasm and/or membrane of the primary cells (Fig. 4 B), indicating that the extracted primary cells were PCP cells. Eight weeks after stereotactic surgery, MRI-T2WI revealed a cystic cavity and solid component of the PCP in the mouse brain, and HE staining revealed tumor cells forming tightly packed squamous epithelial structures and a papillary-like projection inserted into the mouse brain tissue. Beta-catenin, Pan-CK and mutant BRAFv600e, which are classical biomarkers of PCP, are expressed in the cytoplasm and/or cell membrane of tumors in the mouse brain (Fig. 4 C). The MR-T2WI image of the human PCP revealed the cystic cavity and solid tumor, and HE staining revealed that the tumor cells formed tightly packed squamous epithelial structures and papillary-like projections. Moreover, beta-catenin, Pan-CK and mutant BRAFv600e were expressed in the cytoplasm and/or cell membrane of tumor cells in the human brain (Fig. 4 C). Human PCPs served as controls for the mouse PCP model, and the homogeneity of their imaging, histology and tumor biomarker expression findings confirmed the successful establishment of the mouse PCP model, indicating that the model is fully capable of simulating human PCP. To our knowledge, this work presents the first human-originated PCP mouse model, which may provide a reliable instrument for the exploration of therapeutic targets for PCPs.

The therapeutic effect of vemurafenib on the human-originated PCP mouse model

After the mouse model was established, the mice were treated with vemurafenib, a common BRAF inhibitor. After 7 days of therapy, MRI revealed that the BRAFv600e^{+} PCP tumors in the mouse brain significantly shrunk, both in the solid components and cystic cavities of the tumors ($n=7$); however, the BRAFv600e^{-} PCP tumors in the mouse brain continued to grow ($n=6$), as well as the control mice ($n=3$) (Fig. 5 A-B). On the 7th day of therapy, the squamous epithelium of BRAFv600e^{+}

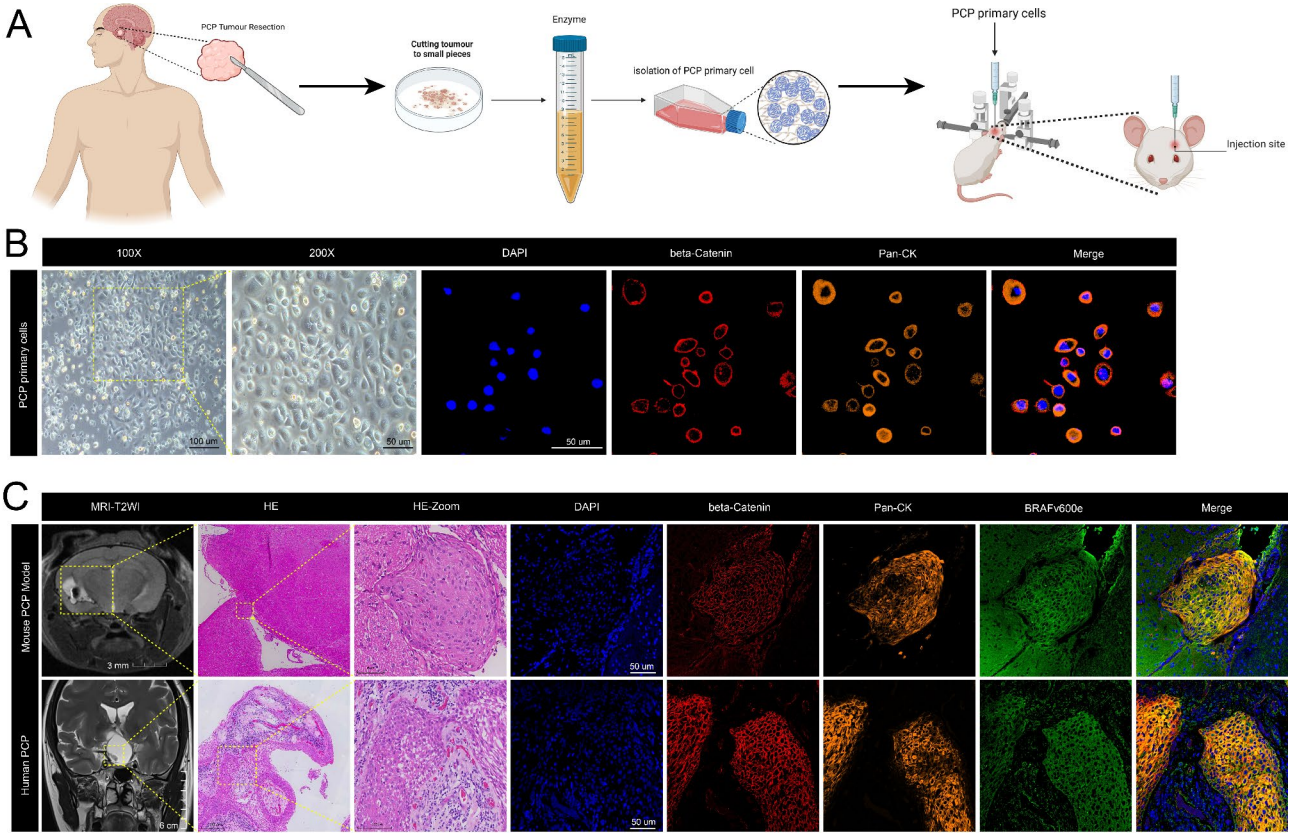

Fig. 4 Establishment and validation of a novel human-originated PCP mouse model. **A**: Schematic representation of the steps involved in the establishment of the novel human-originated PCP mouse model. Fresh PCP tumor tissues were obtained during surgical resection, and the tumor tissue was cut into small, digestible fragments. Primary PCP cells were extracted by adding hyaluronidase and collagenase type I; finally, the primary cells were injected into the brains of the nude mice via stereotactic surgery or stored at -80 °C before pathological diagnosis. **B**: **Validation of primary PCP cells**: The tightly arranged squamous epithelial cells are shown under a light microscope. Beta-catenin and Pan-CK, which are markers for PCP, are expressed in the cytoplasm and/or membrane of primary PCP cells. **C**: **Validation of the PCP mouse model**: 8 weeks after stereotactic surgery, MRI-T2WI revealed mixed-density signals of PCP tumors in the mouse brain ($n=16$), and the cystic cavity (high signal) and solid components of the tumors (equal signal) are shown in the yellow box. HE staining of the section corresponding to this MR image revealed that the tumor was located in the lateral hypothalamus. HE magnification revealed that the tumor cells formed tightly packed squamous epithelial structures and that a papillary-like projection inserted into the mouse brain tissue. The immunofluorescence image corresponds to the HE-stained image. Beta-catenin, Pan-CK and mutant BRAFv600e, which are classical biomarkers of PCPs, are expressed in the cytoplasm and/or cell membrane of mouse tumors ($n=16$). **Human PCP**: MR-T2WI revealed mixed-density signals corresponding to the PCP tumors in the patient's brain ($n=51$); the cystic cavity (high signal) and solid tumor (equal signal) are indicated by yellow boxes. HE staining revealed that the tumor cells formed tightly packed squamous epithelial structures and papillary-like projections. The immunofluorescence image corresponds to the HE-stained image. Beta-catenin, Pan-CK and BRAFv600e mutations were expressed in the cytoplasm and/or cell membrane of the tumors ($n=51$)

PCPs completely disappeared, leaving scar tissue; however, the squamous epithelium of BRAFv600e$^-$ PCPs was still intact in the mouse brain, which was similar to that of the control mice (Fig. 5 C). After treatment for 7 days, in BRAFv600e$^+$ PCPs, the expression of beta-catenin and Pan-CK was negative. However, in BRAFv600e$^-$ PCPs, the expression of beta-catenin and Pan-CK was still positive in the tumor tissue in the mouse brain, which was very similar to that in the control mice (Fig. 5 D). Imaging, histological and pathological changes caused by vemurafenib therapy in the PCP mouse model suggest that the BRAF inhibitor may not have a significant therapeutic effect on BRAFv600e$^-$ PCPs.

The therapeutic effect of anlotinib on the BRAFv600e– PCP mouse model and on BRAFv600e– PCP patients

To identify a new therapeutic target for BRAFv600e$^-$ PCPs, we further excavated the spatial transcriptome sequencing data from the calcifaied PCP patient 1, although his tumor was positive for BRAFv600e. Spatial transcriptome sequencing data indicated that the fibroblasts (cluster 5) surrounding the PCP subclusters specifically expressed PDGFR, an angiogenesis promoter (Fig. 6 A). We validated that, in tumor tissues from BRAFv600e$^+$ PCP patients, the PDGFR was highly expressed in the tumor mesenchyme (Fig. 6 B). Interestingly, in tumor tissues from BRAFv600e$^-$ PCP patients,

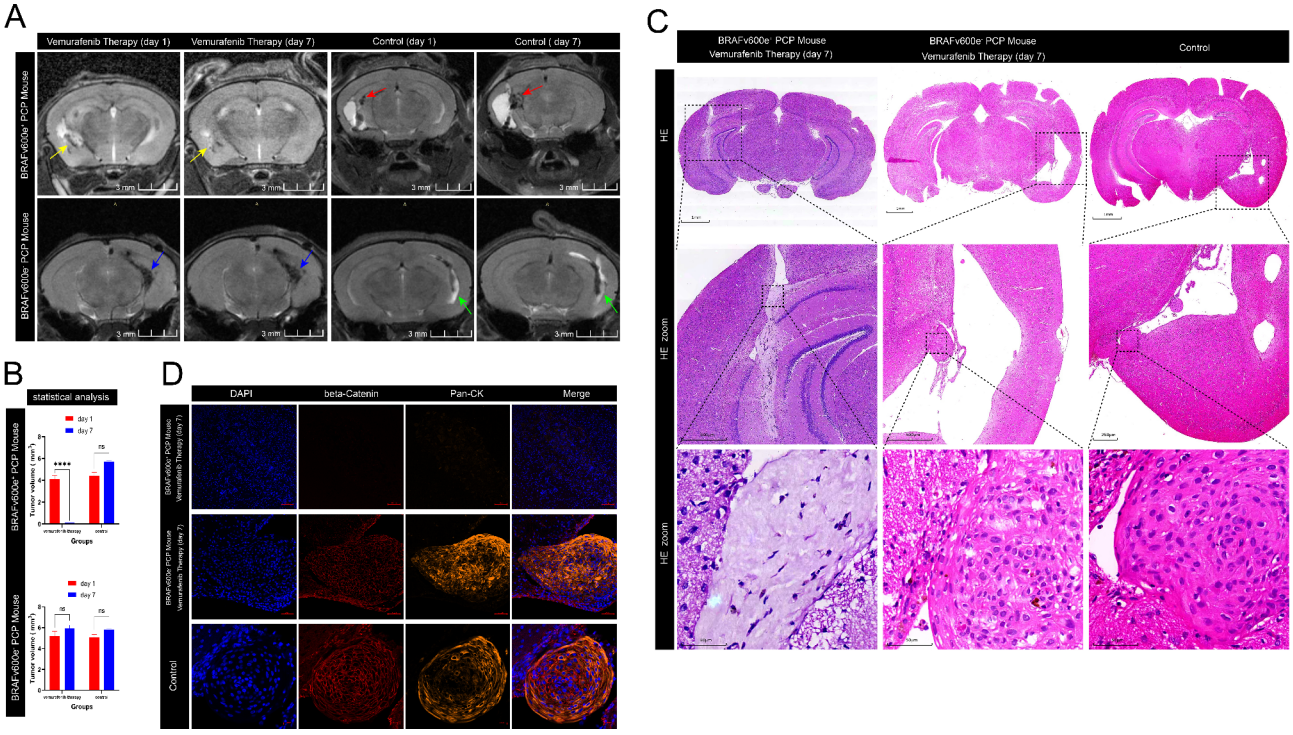

Fig. 5 The therapeutic effect of vemurafenib on the PCP mouse model. **A**: Imaging changes caused by vemurafenib therapy in the PCP mouse model. Vemurafenib therapy on the BRAFv600e^{+} PCP mice: at the 1th day of the therapy, mouse MRI showed cystic cavity and solid component of the tumor(yellow arrow). At the 7th day of the therapy, the cystic cavity and solid component of the tumor had significantly shrunk (yellow arrow) ($n=7$). The tumors in the brains of the control mice (without any treatment) continued to grow, with the red arrow indicating solid tumor components ($n=3$). **Vemurafenib therapy on the BRAFv600e^{-}PCP mice**: at the 1th day of therapy, mouse MRI showed solid component of the tumor (blue arrow). At the 7th day of therapy, the solid component of the tumor continued to grow (blue arrow) ($n=6$). The tumors in the brains of the control mice (without any treatment) also continued to grow (green arrow) ($n=3$). **B**: The average volume of BRAFv600e^{+} PCPs significantly decreased on the 7th day of therapy. ($P<0.001$); however, the average volume of BRAFv600e^{-} PCPs continued to increase on the 7th day of therapy ($P>0.05$). **C**: Histological changes caused by vemurafenib therapy in the PCP mouse model. **Vemurafenib therapy on the BRAFv600e^{+} PCP mice** ($n=7$): at the 7th day of the therapy, the squamous epithelium completely disappeared, leaving scar tissue. **Vemurafenib therapy on the BRAFv600e^{-} PCP mice** ($n=6$): at the 7th day of therapy, the squamous epithelium was still intact in the tumor tissue, which was similar to that of the control mice. **D**: Pathological changes caused by vemurafenib therapy in the PCP mouse model. In BRAFv600e^{+} PCP mice ($n=7$), beta-catenin and Pan-CK expression was negative in the tumor tissue. However, in BRAFv600e^{-} PCP mice ($n=6$), beta-catenin and Pan-CK expression was still positive in the tumor tissue after vemurafenib therapy, which was very similar to the findings in the control mice ($n=3$)

the PDGFR was also abundantly expressed in the tumor mesenchyme, where the fibroblasts were located.

(Fig. 6 C). Furthermore, human PDGFR was positive in tumor mesenchyme of mouse PCP model (Supplementary Fig. 3 B), suggesting that human-derived fibroblasts were co-transplanted with primary PCP cells into the mouse brain. To confirm whether the PDGFR could serve as a new therapeutic target for BRAFv600e^{-} PCPs, the model mice were treated with anlotinib, a common PDGFR inhibitor that acts as an antiangiogenic agent. After 7 days of therapy, MRI revealed that the BRAFv600e^{-} PCP tumors in the brains of the mice significantly shrunk ($n=6$); however, the BRAFv600e^{-} PCP tumors in the control mice (without any treatment) continued to grow ($n=3$) (Fig. 6 D). Furthermore, on the 7th day of therapy, the squamous epithelium of the BRAFv600e^{-} PCP completely disappeared, leaving scar tissue; however, the squamous epithelium was still intact in the tumor tissue of the control mice (Fig. 6 E). After treatment for 7 days, PDGFR and CD31 expression was negative in the tumor tissue of BRAFv600e^{-} PCP mice ($n=6$). However, PDGFR and CD31(a marker of vascular endothelial cell) expression was still positive in the mesenchyme of tumor tissue in control mice ($n=3$) (Supplementary Fig. 3 C).These findings suggest that anlotinib targeting PDGFR may inhibit the formation of nourishing vessels in PCP tumors.

Calcified PCP Patient 2 and calcified PCP Patient 4, the BRAFv600e mutation was negative in their tumors, underwent tumor recurrence after surgery. Based on the above results, our team initiated a phase 1 clinical trial of anlotinib therapy in these patients with BRAFv600e^{-} PCP. After 3 months of anlotinib capsule therapy, the tumors essentially disappeared, leaving the pituitary intact, and after 24 months of follow-up, there was no tumor

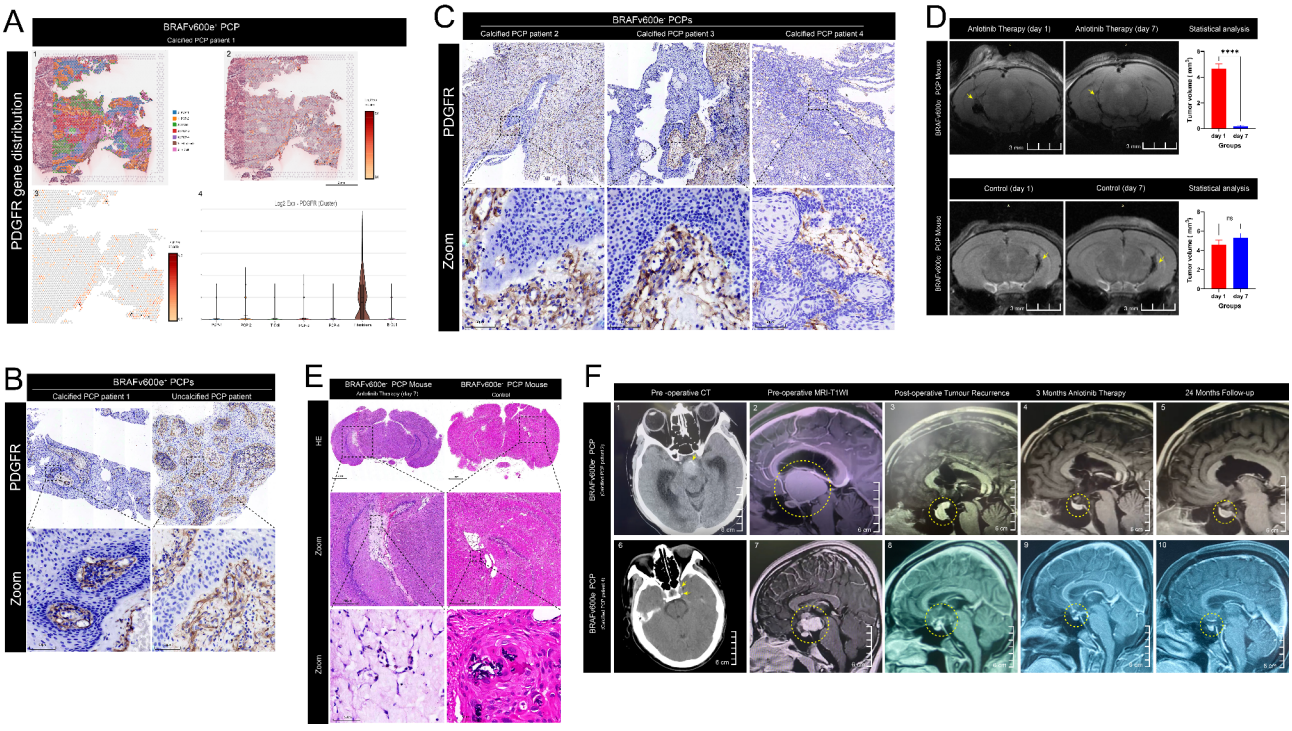

Fig. 6 The therapeutic effect of anlotinib on the BRAFv600e⁻ PCP mouse model and BRAFv600e⁻ PCP patients. **A**: Spatial transcriptome sequencing data from the calcifaied PCP patient 1, who carried the BRAFv600e mutation, indicated that the fibroblasts (cluster 5) specifically expressed PDGFR. A1: Fibroblasts (Cluster 5) surrounding PCP cells on a spatial map. A2-A4: PDGFR is the most specifically expressed gene in fibroblasts (cluster 5). **B**: In tumor tissues from BRAFv600e^{+} PCP patients, PDGFR was highly expressed in the tumor mesenchyme. **C**: In tumor tissues from BRAFv600e⁻ PCP patients, PDGFR was also abundantly expressed in the tumor mesenchyme, where the fibroblasts were located. **D**: Imaging changes caused by anlotinib (a PDGFR inhibitor) therapy in BRAFv600e⁻ PCP mice. At the 1th day of therapy, mouse MRI showed solid component of the tumor (yellow arrow). At the 7th day of therapy, the solid component of the tumor had significantly shrunk (yellow arrow) ($n=6$). The tumors in the brains of the control mice (without any treatment) continued to grow, with the yellow arrow indicating the tumor ($n=3$). **E**: Histological changes caused by anlotinib therapy in BRAFv600e⁻ PCP mice. At the 7th day of therapy, the squamous epithelium had completely disappeared, leaving scar tissue ($n=6$); however, the squamous epithelium was still intact in the tumor tissue of the control mice ($n=3$). **F**: Detailed presentation of two patients with BRAFv600e⁻ PCP from the early stage of the disease to clinical cure. **1–5: Calcified PCP Patient 2 (male, 21 years old), negative for the BRAFv600e mutation**. **1**: The yellow arrow in the preoperative CT image indicates tumor calcification. **2**: The yellow dotted box in the preoperative MR-T1WI enhancement image indicates the tumor. **3**: The patient underwent tumor resection surgery, and the tumor recurred 1 year after surgery (indicated by the yellow dotted box). **4**: After tumor recurrence, the patient received oral treatment with anlotinib capsules, and the tumor essentially disappeared after 3 months of treatment, leaving the pituitary intact (indicated by the yellow dotted box). **5**: After 24 months of follow-up, there was no tumor recurrence (yellow dotted box). **6–10: Calcified PCP Patient 4 (female, 18 years old), negative for the BRAFv600e mutation**. **6**: The yellow arrow in the preoperative CT image indicates tumor calcification. **7**: The yellow dotted box in the preoperative MR-T1WI enhancement image indicates the tumor. **8**: The patient underwent tumor resection surgery, and the tumor recurred 14 months after surgery (indicated by the yellow dotted box). **9**: After tumor recurrence, the patient received oral treatment with anlotinib capsules, and the tumor essentially disappeared after 3 months of treatment, leaving the pituitary intact (indicated by the yellow dotted box). **10**: After 24 months of follow-up, there was no tumor recurrence (yellow dotted box)

recurrence (Fig. 6 F). These findings suggest that anlotinib may have a therapeutic effect on BRAFv600e⁻ PCPs.

Discussion

Calcification in PCPs is very rare, and the mechanism is still unclear. In this study, new types of PCP cells were identified through spatial transcriptome sequencing on a calcified PCP tissue, and it was found that all calcified PCP cell subtypes have unique functions. The PCP-1 subcluster presented high expression of SLPI, which was previously shown to be secreted mainly by epithelial cells and to protect epithelial tissues from serine proteases [17–20], suggesting that the PCP-1 cell subtype may protect the squamous epithelial structures of the PCP from immune cells via SLPI. The PCP-2 subcluster showed specific high expression of KRT14, which encodes the type 1 keratin that forms the epithelial cell skeleton and promotes tight junctions between epithelial cells [21], suggesting that the formation of PCP squamous epithelial structures connected by tight junctions may be related to KRT14 expression. In addition, the PCP-2 and PCP-3 cell subtypes specifically express the ODAPH, RUNX2 and BMP2 genes, which have been shown to promote calcification and odontogenesis in ACPs [22–24], and have been validated in all calcified PCPs in this study; however, all uncalcified PCPs do

not express these genes, implying that the calcification-promoting genes BMP2, RUNX2 and ODAPH may play essential roles in PCP calcification. The PCP-4 subcluster specifically expressed high levels of MMP12 and KRT13, which promote epithelial cell-to-cell adhesion and proliferation [25, 26], implying that the PCP-4 subcluster may be a major contributor to the proliferation of PCP cells. Pseudotime analysis revealed that PCP subclusters undergo differentiation from Cluster 0 → Cluster 4 → Cluster 3 → Cluster 1 during development, and the corresponding biological feature is epithelial formation → cell proliferation → calcification → tight junction formation, indicating that the PCP-3 subcluster (Cluster 3) may have the potential to differentiate toward calcification during development. This study revealed, for the first time, that calcified PCP subclusters differentiate in 3 directions during their differentiation: cell proliferation, senescence, and calcification. Notably, senescence and calcification are typical biological features of ACP cells, and calcification is a process that occurs after cell death and is a senescence-dependent pathological change [27], implying that calcification may be a result of cell senescence in calcified PCPs. Pathologically, ACPs are characterized by clustered cells (epithelial whorls), palisading epithelium, stellate reticulum, wet keratin, cystic cavities, calcifications, ghost cells without nuclei, and nuclear beta-catenin, which are generally considered a basis for the pathologic diagnosis of ACPs [28]. This study revealed that calcified PCPs presented squamous epithelium, wet keratin, calcifications and ossifications but not the epithelial whorls or stellate reticulum characteristic of ACPs. More importantly, beta-catenin is localized to the cell membrane rather than the nucleus in all calcified PCPs, furthermore, the CTNNB1 mutation in exon 3 was negative in all calcified PCPs, which is strong evidence that they are PCPs rather than ACPs [10]. These phenomena suggest that calcified PCPs may have a similar pathogenesis to ACPs.

Although current clinical trials have reported the successful treatment of PCPs with BRAFv600e inhibitors [1, 29], approximately 10% of PCPs are negative for the BRAFv600e mutation [30, 31], implying that BRAFv600e inhibitors may not have a significant therapeutic effect on these PCPs. Unfortunately, no studies have reported on BRAFv600e$^-$ PCPs, and these PCPs seem to be neglected because they are very rare. This study revealed for the first time that most of calcified PCPs were negative for the BRAFv600e mutation. A recent study revealed that BRAFv600e$^+$ PCPs may be formed by Rax + tanycytes with a BRAFv600e mutation in the median eminence of the hypothalamus [32]; however, our findings in this study support that the BRAFv600e$^-$ PCPs may be completely different from BRAFv600e$^+$ PCPs and may arise from the metaplasia of cells remaining from embryonic Rathke cleft cysts (RCCs), similar to ACPs. These findings imply that BRAFv600e$^-$ PCPs and ACPs may be twin brothers born from RCCs.

To date, no animal model of human PCP-related tumor formation in animal brain tissue has been reported. Although successful induction of PCP tumors in the mouse hypothalamus via BRAF transgenesis has been reported, this tumor is of mouse origin rather than of human origin [9, 33]. In this study, a novel human-origin PCP mouse model was established, and it was identical to human PCPs in terms of imaging, histology and tumor biomarker expression, confirming the successful establishment of the model and indicating that the model is fully capable of simulating human PCPs. To our knowledge, this is the first stable mouse PCP model of human origin, which may provide a reliable basis for the exploration of new therapeutic targets for PCPs. Recent clinical trials have demonstrated significant reductions in PCP tumor volume after treatment with BRAF inhibitors [30, 34, 35]; however, the changes in pathology induced by therapy have rarely been captured. In this study, changes in the imaging, histology and pathology of BRAFv600e$^+$ PCP tumors after vemurafenib (BRAF inhibitor) therapy were observed in the mouse brain. Moreover, this study revealed for the first time that BRAFv600e$^-$ PCPs in mouse brains do not respond to vemurafenib therapy in vivo, confirming that BRAF inhibitors may not have a significant therapeutic effect on BRAFv600e$^-$ PCPs.

The glial reaction tissue around ACP cells is enriched with glial cells and fibroblasts [5, 14], acting as a "protective armor" for the ACP to protect it from cytotoxic T-cell surveillance [36]. In many cancers, fibroblasts are a barrier that protects cancer cells from elimination by immune cells [37]. In this study, in terms of spatial distribution, fibroblasts were located around the PCP tumor cells, showing a tendency to surround the tumor cells, a pattern very similar to that of ACP cells surrounded by glial reaction tissue, implying that the fibroblasts surrounding PCP tumor cells may serve as a protective armor to prevent PCP cells from being attacked by immunocytes. Moreover, fibroblasts also contribute to angiogenesis, forming nourishing vessels of tumors in many cancers [38–41]. However, the role of fibroblasts in PCPs remains unknown. In this study, spatial transcriptome analysis revealed that fibroblasts specifically enriched PDGFR, an angiogenesis promoter [42, 43]. PDGFR was highly expressed in the tumor mesenchyme, where the fibroblasts were located, both on BRAFv600e$^+$ PCPs and on BRAFv600e$^-$ PCPs, suggesting that PDGFR may be a novel therapeutic target of BRAFv600e$^-$ PCPs.

We identified a PDGFR inhibitor, anlotinib, which is widely used in the clinic for the treatment of non-small cell lung cancer and acts as an antiangiogenic agent to block the formation of nourishing vessels in tumors [44,

45]. However, anlotinib has not been reported to be used to treat PCPs. The PCP mouse model in this study revealed that anlotinib may have a significant therapeutic effect on BRAFv600e⁻ PCPs by targeting PDGFR, and this success in vivo led us to initiate a phase 1 clinical trial for anlotinib therapy in BRAFv600e⁻ PCP patients. In this study, two patients with BRAFv600e⁻ PCPs received oral therapy with anlotinib capsules for 3 months, and their tumors almost completely disappeared. There was no tumor recurrence at the 24-month follow-up after therapy stopped, and patients' quality of life was preserved. To our knowledge, these are the first cases of BRAFv600e⁻ PCPs to be cured by anlotinib in the world thus far, suggesting that anlotinib may have a significant therapeutic effect on BRAFv600e⁻ PCPs. We believe that treating PCPs with a combination of a BRAF inhibitor and anlotinib may soon be recognized as an effective means of curing this difficult disease.

Limitations

This study has the same inherent limitations related to sequencing depth that all mononuclear and spatial RNA-seq studies have; that is, changes in the expression of low-abundance transcripts cannot be detected. The current sample size was chosen for practical reasons, including cost. Although the sample size was small, we verified the findings through a variety of experimental methods and obtained similar results. As the cost of spatial RNA-seq research decreases, future research may verify our findings in a larger sample. PCP primary cells isolated from the calcified PCP tumor tissue are hardly to survive in vitro, so we are unable to validate the pseudotime analysis.Although we found that anlotinib targeting PDGFR may have a significant therapeutic effect on BRAFv600e⁻ PCPs by generating PDX, its mechanism in human body is still unknown, mainly because we cannot get tumor samples after treatment. Given the very rare incidence of PCPs, we reported only 2 cases of recurrent BRAFv600e⁻ PCPs with a significant response to anlotinib. We believe that reports from colleagues worldwide on the treatment of BRAFv600e⁻ PCPs with anlotinib will further corroborate our findings.

Conclusion

This study revealed for the first time that BRAFv600e⁻ PCPs are characterized by calcification and do not respond to the BRAF inhibitor vemurafenib, and for which the angiogenesis inhibitor anlotinib may have a significant therapeutic effect.

Supplementary Information

The online version contains supplementary material available at https://doi.org/10.1186/s40478-025-01972-7.

Supplementary Material 1

Supplementary Material 2: **fig. 1**: heatmap of PCP Spatial transcriptional sequencing cell clustering. A Heatmap demonstrating the expression levels of the top 10 marker genes specifically expressed by each cluster. Each row of the graph represents a marker, and each column represents a spot in each cluster. A deeper red color indicates a higher expression level of the gene in the cluster. PCP-1 (Cluster 0) presented specifically high expression of SLPI, and PCP-2 (Cluster 1) presented specifically high expression of KRT14. PCP-3 (Cluster 3) presented specifically high expression of the keratinogenesis-promoting gene LAMA3 and the enamel formation-promoting gene ODAPH. PCP-4 cells (Cluster 4) presented specifically high expression of MMP12 and KRT13, which promote cell adhesion and proliferation. T cells (Cluster 2) presented specifically high expression of MALAT1. Fibroblasts (Cluster 5) specifically expressed the MGP and VIM. B cells (Cluster 6) presented specifically high expression of IGHG1 and IGKC, genes encoding immunoglobulins.

Supplementary Material 3: **fig. 2**: genes promoting calcification were enriched in the PCP subcluster on the calcified PCP tumor tissue. A-C Spatial distribution of the calcification-promoting marker genes RUNX2, ODAPH, and BMP2 in calcified PCP tumor samples. Darker colors represent more significant gene enrichment. D-F: Violin plot of the calcification-associated marker genes RUNX2, ODAPH, and BMP2, which were enriched in calcified PCP-type tumor samples. G: Validation of BMP2, ODAPH, and RUNX2 in calcified PCP tumor samples. BMP2, RUNX2 and ODAPH were expressed on calcified PCPs (***n***=4) as well as on the ACPs (***n***=17). However, the expression of BMP2, RUNX2 and ODAPH was negative in the uncalcified PCPs (***n***=47).

Supplementary Material 4: **fig. 3**: anlotinib May inhibit the formation of tumor-feeding vessels in BRAFv600e– PCP tumors in mice brain. A Detection of CTNNB1 gene mutation in exon 3. The CTNNB1 mutation was positive in ACP tumor tissue (black arrow indicated double wave peaks, suggesting mutation) (***n***=17), but in the calcified PCPs, the CTNNB1 mutation was negative (***n***=4). B: Human-derived PDGFR was positive in tumor mesenchyme of human PCPs (***n***=51) and mouse PCP model (***n***=25). C: Pathological changes caused by anlotinib therapy in the BRAFv600e⁻ PCP mouse model. At the 7th day of therapy, PDGFR and CD31 expression was negative in the tumor tissue (***n***=6). However, PDGFR and CD31 expression was still positive in the mesenchyme of tumor tissue in control mice (***n***=3).

Acknowledgements

The authors thank Lin Yin and Bihui Zhang from Accuramed Technology (Guangzhou, China) for providing assistance with the spatial RNA-seq bioinformatics analysis. The authors thank American Journal Experts (AJE) for providing language editing services.

Author contributions

J.P: Conceived and designed the study and guided the clinical trial. S.Q: Supervised and guided the study. Q.S: Supervised the data validation. Y.A: Completed the experiments and wrote the original manuscript. H.L: Summarized and analyzed the data. Y.Z: Assisted in completing experiments. S.W: Assisted in data analysis and writing manuscript. J.X.P: Supervised the writing process of the article. J.N and C.M: Prepared the experimental reagents, consumables and analysis tools. K.C, S.C and N.L: Assisted in data validation. C.L: Prepared the mouse MRI imaging. Y.C: Assisted in the clinical trial. S.Q.Q: Collected the tumor specimens. Y.W, M.Z and J.M: Collected the patients information. F.M and J.C: Prepared the experimental equipments. Y.A, H.L, Y.Z and S.W contributed equally to this work and should be considered co-first authors.

Funding

(1) National Natural Science Foundation of China: A study on the Mechanism of which beta-amyloid regulates the development of adamantinomatous craniopharyngioma by inducing senescence (32400973). (2) National Natural Science Foundation of China: Over-activation of cholesterol metabolism via AMPK-SREBP2 pathway in adamantinomatous craniopharyngioma induces microglial inflammatory response (81972352). (3) Natural Science Foundation of Guangdong Province, China (2024A1515010060).

Data availability
The Spatial Transcriptome Sequencing data are accessible through NCBI Sequence Read Archive (SRA) under the accession number SRR29385909. All data generated and/or analyzed during the current study are available from the corresponding author on reasonable request.

Declarations

Ethical approval and consent to participate
(1) Animals: All operations about animals were approved by the Laboratory Animal Center and the Ethics Committee of Southern Medical University and complied with the National Institute of Health Guidelines for the Protection and Use of Laboratory Animals (NFYY-2020-0935). (2) Human subjects: The patients all signed an informed consent form expressing their willingness to allow the use of the excised tumor tissue for scientific research, and the study received approval from the Ethics Committee of Southern Medical University. (3) Clinical Trial: The trial was approved by the Ethics Committee of Nanfang Hospital, Southern Medical University and registered at ClinicalTrial.gov (identifier: NCT00949156). Patients consented to participate in the trial and consented to publication of the outcomes. The work described has been carried out in accordance with The Code of Ethics of the World Medical Association (Declaration of Helsinki).

Consent for publication
All the authors have read the original manuscript and consented to publish it.

Competing interests
The authors declare no competing interests.

Author details
[1]Department of Neurosurgery, Nanfang Hospital, Southern Medical University, Guangzhou, China
[2]Department of Neurosurgery, The First People's Hospital of Foshan, Foshan, China
[3]First Clinical Medical College, Southern Medical University, Guangzhou, China
[4]Department of Neurosurgery, Jinling Hospital, Xuanwu, China
[5]Department of Neurology, State Key Laboratory of Complex Severe and Rare Diseases, Peking Union Medical College Hospital, Chinese Academy of Medical Sciences and Peking Union Medical College, Beijing, China
[6]Central Laboratory, Southern Medical University, Guangzhou, Guangdong, China
[7]Guangdong Provincial Key Laboratory of Bone and Joint Degeneration Diseases, Department of Cell Biology, School of Basic Medical Sciences, Southern Medical University, Guangzhou, China

Received: 27 December 2024 / Accepted: 22 February 2025
Published online: 03 March 2025

References

1. Muller HL, Merchant TE, Warmuth-Metz M, Martinez-Barbera JP, Puget S (2019) Craniopharyngioma. Nat Rev Dis Primers 5:75
2. Mete O, Lopes MB (2017) Overview of the 2017 WHO classification of pituitary tumors. Endocr Pathol 28:228–243
3. Muller HL (2020) The diagnosis and treatment of craniopharyngioma. Neuroendocrinology 110:753–766
4. Liu Y, Wang CH, Fan J, Peng JX, Pan J, Zhang X, Qi ST (2021) Establishing a papillary craniopharyngioma cell line by SV40LT-mediated immortalization. Pituitary 24:159–169
5. Prince EW, Apps JR, Jeang J, Chee K, Medlin S, Jackson EM, Dudley R, Limbrick D, Naftel R, Johnston J et al (2024) Unraveling the complexity of the senescence-associated secretory phenotype in adamantinomatous craniopharyngioma using multimodal machine learning analysis. Neuro Oncol 26:1109–1123
6. Apps JR, Carreno G, Gonzalez-Meljem JM, Haston S, Guiho R, Cooper JE, Manshaei S, Jani N, Holsken A, Pettorini B et al (2018) Tumour compartment transcriptomics demonstrates the activation of inflammatory and odontogenic programmes in human adamantinomatous craniopharyngioma and identifies the MAPK/ERK pathway as a novel therapeutic target. Acta Neuropathol 135:757–777
7. Ainiwan Y, Chen Y, Mao C, Peng J, Chen S, Wei S, Qi S, Pan J (2022) Adamantinomatous craniopharyngioma cyst fluid can trigger inflammatory activation of microglia to damage the hypothalamic neurons by inducing the production of beta-amyloid. J Neuroinflammation 19:108
8. Wang C, Zhang H, Fan J, Li Q, Guo R, Pan J, Liu Y, Peng J, Zhu Q, Feng Y et al (2023) Inhibition of integrated stress response protects against lipid-induced senescence in hypothalamic neural stem cells in adamantinomatous craniopharyngioma. Neuro Oncol 25:720–732
9. Mu W, Li S, Xu J, Guo X, Wu H, Chen Z, Qiao L, Helfer G, Lu F, Liu C, Wu QF (2021) Hypothalamic Rax(+) tanycytes contribute to tissue repair and tumorigenesis upon oncogene activation in mice. Nat Commun 12:2288
10. Holsken A, Sill M, Merkle J, Schweizer L, Buchfelder M, Flitsch J, Fahlbusch R, Metzler M, Kool M, Pfister SM et al (2016) Adamantinomatous and papillary craniopharyngiomas are characterized by distinct epigenomic as well as mutational and transcriptomic profiles. Acta Neuropathol Commun 4:20
11. Prieto R, Barrios L, Pascual JM (2022) Papillary craniopharyngioma: A type of tumor primarily impairing the Hypothalamus - A comprehensive Anatomo-Clinical characterization of 350 Well-Described cases. Neuroendocrinology 112:941–965
12. Apps JR, Gonzalez-Meljem JM, Guiho R, Pickles JC, Prince E, Schwalbe E, Joshi N, Stone TJ, Ogunbiyi O, Chalker J et al (2024) Recurrent adamantinomatous craniopharyngiomas show MAPK pathway activation, clonal evolution and rare TP53-loss-mediated malignant progression. Acta Neuropathol Commun 12:127
13. Louis DN, Perry A, Wesseling P, Brat DJ, Cree IA, Figarella-Branger D, Hawkins C, Ng HK, Pfister SM, Reifenberger G et al (2021) The 2021 WHO classification of tumors of the central nervous system: a summary. Neuro Oncol 23:1231–1251
14. Chen Y, Liu X, Ainiwan Y, Li M, Pan J, Chen Y, Xiao Z, Wang Z, Xiao X, Tang J et al (2024) Axl as a potential therapeutic target for adamantinomatous craniopharyngiomas: based on single nucleus RNA-seq and Spatial transcriptome profiling. Cancer Lett 592:216905
15. Xu C, Wu J, Ye J, Si Y, Zhang J, Wu B, Pan L, Fu J, Ren Q, Xie S et al (2024) Multiomics integration-based immunological characterizations of adamantinomatous craniopharyngioma in relation to keratinization. Cell Death Dis 15:439
16. Wang X, Lin J, Liu H, Zhao C, Tu Z, Xu D, Zhang E, Zhou Z, Qi X, Wang X, Lin Z (2024) Single-cell and Spatial sequencing identifies senescent and germinal tumor cells in adamantinomatous craniopharyngiomas. Cell Biosci 14:112
17. Raundhal M, Morse C, Khare A, Oriss TB, Milosevic J, Trudeau J, Huff R, Pilewski J, Holguin F, Kolls J et al (2015) High IFN-gamma and low SLPI mark severe asthma in mice and humans. J Clin Invest 125:3037–3050
18. Itaoka N, Nagamatsu T, Schust DJ, Ichikawa M, Sayama S, Iwasawa-Kawai Y, Kawana K, Yamashita T, Osuga Y, Fujii T (2015) Cervical expression of Elafin and SLPI in pregnancy and their association with preterm labor. Am J Reprod Immunol 73:536–544
19. Sibila O, Perea L, Albacar N, Moises J, Cruz T, Mendoza N, Solarat B, Lledo G, Espinosa G, Barbera JA et al (2022) Elevated plasma levels of epithelial and endothelial cell markers in COVID-19 survivors with reduced lung diffusing capacity six months after hospital discharge. Respir Res 23:37
20. Zhang X, Liu SS, Ma J, Qu W (2023) Secretory leukocyte protease inhibitor (SLPI) in cancer pathophysiology: mechanisms of action and clinical implications. Pathol Res Pract 248:154633
21. Zhang X, Yin M, Zhang LJ (2019) Keratin 6, 16 and 17-Critical barrier alarmin molecules in skin wounds and psoriasis. Cells, p 8
22. Liang T, Hu Y, Kawasaki K, Zhang H, Zhang C, Saunders TL, Simmer JP, Hu JC (2021) Odontogenesis-associated phosphoprotein Truncation blocks ameloblast transition into maturation in Odaph(C41*/C41*) mice. Sci Rep 11:1132
23. Song-Tao Q, Xiao-Rong Y, Jun P, Yong-Jian D, Jin L, Guang-Long H, Yun-Tao L, Jian R, Xiang-Zhao L, Jia-Ming X (2014) Does the calcification of adamantinomatous craniopharyngioma resemble the calcium deposition of osteogenesis/odontogenesis? *Histopathology*. 64:336–347
24. Yan X, Kang D, Lin Y, Qi S, Jiang C (2022) CBX4-dependent regulation of HDAC3 nuclear translocation reduces Bmp2-induced osteoblastic differentiation and calcification in adamantinomatous craniopharyngioma. Cell Commun Signal 20:3
25. Zuo A, Li J, Weng S, Xu H, Zhang Y, Wang L, Xing Z, Luo P, Cheng Q, Li J et al (2024) Integrated exploration of epigenetic dysregulation reveals a Stemness/EMT subtype and MMP12 linked to the progression and prognosis in hepatocellular carcinoma. J Proteome Res 23:1821–1833

26. Yu D, Chen C, Sun L, Wu S, Tang X, Mei L, Lei C, Wang D, Wang X, Cheng L, Li S (2023) KRT13-expressing epithelial cell population predicts better response to chemotherapy and immunotherapy in bladder cancer: comprehensive evidences based on BCa database. Comput Biol Med 158:106795
27. Santos JMA, Laize V, Gavaia PJ, Conceicao N, Cancela ML (2023) Zebrafish models to study ectopic calcification and Calcium-Associated pathologies. Int J Mol Sci 24
28. Rumayor A, Carlos R, Kirsch HM, de Andrade BA, Romanach MJ, de Almeida OP (2015) Ghost cells in Pilomatrixoma, craniopharyngioma, and calcifying cystic odontogenic tumor: histological, immunohistochemical, and ultrastructural study. J Oral Pathol Med 44:284–290
29. Juratli TA, Jones PS, Wang N, Subramanian M, Aylwin SJB, Odia Y, Rostami E, Gudjonsson O, Shaw BL, Cahill DP et al (2019) Targeted treatment of papillary craniopharyngiomas harboring BRAF V600E mutations. Cancer 125:2910–2914
30. Calvanese F, Jacquesson T, Manet R, Vasiljevic A, Lasolle H, Ducray F, Raverot G, Jouanneau E (2022) Neoadjuvant B-RAF and MEK inhibitor targeted therapy for adult papillary craniopharyngiomas: A new treatment paradigm. Front Endocrinol (Lausanne) 13:882381
31. Malgulwar PB, Nambirajan A, Pathak P, Faruq M, Suri V, Sarkar C, Jagdevan A, Sharma BS, Sharma MC (2017) Study of beta-catenin and BRAF alterations in adamantinomatous and papillary craniopharyngiomas: mutation analysis with immunohistochemical correlation in 54 cases. J Neurooncol 133:487–495
32. Li S, Li W, Miao Y, Gao M, Jia Y, Chen Z, Chen X, Pan T, Zhang S, Xing Z et al (2024) Modeling craniopharyngioma for drug screening reveals a neuronal mechanism for tumor growth. Sci Transl Med 16:eadn6763
33. Lin B, Ye Z, Cao Z, Ye Z, Yu Y, Jiang W, Guo S, Melnikov V, Zhou P, Ji C et al (2024) Integrated Microbiome and metabolome analysis reveals Hypothalamic-Comorbidities related signatures in craniopharyngioma. Adv Sci (Weinh) 11:e2400684
34. Brastianos PK, Twohy E, Geyer S, Gerstner ER, Kaufmann TJ, Tabrizi S, Kabat B, Thierauf J, Ruff MW, Bota DA et al (2023) BRAF-MEK Inhibition in newly diagnosed papillary craniopharyngiomas. N Engl J Med 389:118–126
35. Rostami E, Witt Nystrom P, Libard S, Wikstrom J, Casar-Borota O, Gudjonsson O (2017) Recurrent papillary craniopharyngioma with BRAFV600E mutation treated with neoadjuvant-targeted therapy. Acta Neurochir (Wien) 159:2217–2221
36. Coy S, Rashid R, Lin JR, Du Z, Donson AM, Hankinson TC, Foreman NK, Manley PE, Kieran MW, Reardon DA et al (2018) Multiplexed Immunofluorescence reveals potential PD-1/PD-L1 pathway vulnerabilities in craniopharyngioma. Neuro Oncol 20:1101–1112
37. Shahvali S, Rahiman N, Jaafari MR, Arabi L (2023) Targeting fibroblast activation protein (FAP): advances in CAR-T cell, antibody, and vaccine in cancer immunotherapy. Drug Deliv Transl Res 13:2041–2056
38. Kalluri R (2016) The biology and function of fibroblasts in cancer. Nat Rev Cancer 16:582–598
39. Verginadis II, Avgousti H, Monslow J, Skoufos G, Chinga F, Kim K, Leli NM, Karagounis IV, Bell BI, Velalopoulou A et al (2022) A stromal integrated stress response activates perivascular cancer-associated fibroblasts to drive angiogenesis and tumour progression. Nat Cell Biol 24:940–953
40. Zeng H, Hou Y, Zhou X, Lang L, Luo H, Sun Y, Wan X, Yuan T, Wang R, Liu Y et al (2022) Cancer-associated fibroblasts facilitate premetastatic niche formation through LncRNA SNHG5-mediated angiogenesis and vascular permeability in breast cancer. Theranostics 12:7351–7370
41. Li P, Zhang H, Chen T, Zhou Y, Yang J, Zhou J (2024) Cancer-associated fibroblasts promote proliferation, angiogenesis, metastasis and immunosuppression in gastric cancer. Matrix Biol 132:59–71
42. Taeger J, Moser C, Hellerbrand C, Mycielska ME, Glockzin G, Schlitt HJ, Geissler EK, Stoeltzing O, Lang SA (2011) Targeting FGFR/PDGFR/VEGFR impairs tumor growth, angiogenesis, and metastasis by effects on tumor cells, endothelial cells, and pericytes in pancreatic cancer. Mol Cancer Ther 10:2157–2167
43. Lin H, Lin R, Hou J, Zhu C, Liu G, Lin Y, Su J, Yang M, Yang B, Ma Y et al (2024) Targeting endothelial PDGFR-beta facilitates angiogenesis-associated bone formation through the PAK1/NICD axis. J Cell Physiol 239:e31291
44. Cords L, Engler S, Haberecker M, Ruschoff JH, Moch H, de Souza N, Bodenmiller B (2024) Cancer-associated fibroblast phenotypes are associated with patient outcome in non-small cell lung cancer. Cancer Cell 42:396–412e395
45. Shen G, Zheng F, Ren D, Du F, Dong Q, Wang Z, Zhao F, Ahmad R, Zhao J (2018) Anlotinib: a novel multi-targeting tyrosine kinase inhibitor in clinical development. J Hematol Oncol 11:120

Publisher's note